*Journal of Machine Engineering, 2026, Vol. 26*
*ISSN 1895-7595 (Print) ISSN 2391-8071 (Online)*

Received: *28 January 2026* /Accepted: *27 April 2026* / Published online: *26 May 2026*

*pentapod, laser scanner,*
*additive manufacturing,*
*point cloud*

Matthias SCHÄFER[1*],
Tim UNGETHÜM[1],
Hans Christian SCHMALE[1]

# ENHANCEMENT OF A HYBRID MANUFACTURING SYSTEM BASED ON A PENTAPOD ARCHITECTURE BY 3D SURFACE MEASUREMENT USING A LASER SCANNER

Arc-based additive manufacturing (DED-Arc) is a widespread, well established, near-net-shape manufacturing process. However, achieving the desired geometry is still a challenging task. Interlayer machining is a common method to overcome such challenges. Therefore, multi-axis kinematics in the form of a pentapod are predestined because of their high stiffness and accuracy. Extensive research has concluded that monitoring the manufacturing process is crucial to increase the level of automation in manufacturing towards full automation and also to combine the additive and subtractive process in a more intelligent way. Laser scanners are suitable tools for this purpose. In this article, the authors present how a laser scanner can be integrated into a pentapod architecture and how its kinematic peculiarity has to be considered. At first, the resulting measurement error is shown if the implicit forced rotation of the laser scanner caused by the pentapod's mechanical concept is neglected and how to consider the rotation using homogeneous coordinates. Finally, the achieved accuracy of the measurement system is evaluated.

## 1. INTRODUCTION

Additive manufacturing enables the production of components that can only be manufactured with increased effort or not at all using conventional subtractive or forming and reshaping manufacturing principles (e.g. turning, milling, pressing, casting, etc.). According to ISO/ASTM 52900 [1], one process category of additive manufacturing are processes with a directed deposition of energy (Direct Energy Deposition – DED) to join the base and additional materials by melting them and thus build up a component layer by layer [2]. The material is deposited in layers whose normal vector corresponds to the build-up direction and is usually directed against gravity. One possibility for directed energy deposition is arc welding (DED-Arc). In the case of DED-Arc, the material transfer takes place in liquid form, in that the additional material is melted by the arc and then solidifies on the base material. In this way, a three-dimensional geometry is created.

[1] Chair of Joining Technology and Assembly, Faculty of Mechanical Science and Engineering, Dresden University of Technology, Germany
[*] E-mail: matthias.schaefer@tu-dresden.de
https://doi.org/10.36897/jme/221137

In addition to some advantages, for example the higher energy efficiency [3] and build-up rate compared to powder bed fusion processes or the build-up of large-volume components [4], additive manufacturing based on DED-Arc also has disadvantages. A significant disadvantage is that the occurrence of geometric deviations during production cannot be reliably avoided. In the context of this publication, geometric deviations refer to deviations in the millimeter range between the desired and actual geometry of a component that may occur during the layer-by-layer build-up. Examples of this are

- a deviation between the planned and actual layer height,
- tilting of the build plane,
- the tilting up of the ends of thin-walled structures,
- or local bulges or dents within a layer.

Xu et al. [5] stated that, since the build-up is executed layer by layer, the surface quality of the previous layer heavily influences the quality of the subsequent layer. Small deviations can lead to significant defects or the loss of the component as manufacturing progresses. For this reason, many research studies deal with the optimization of the layer shape, for example by exact control of the bead geometry or by improving the path planning and slicing algorithms [6]. For instance, Suryakumar et al. [7], Hu et al. [8], Raffaeli et al. [9] or Foorginejad et al. [10] worked on multi-bead overlapping models to optimize layer quality, whereas Rauch et al. [11] used varying layer heights to build up bent, thin-walled geometries. Although all these investigations reduce the frequency and severity of geometric deviations, they cannot be completely avoided.

To compensate for deviations during the build-up, the last deposited layer can be machined in a subtractive intermediate step [12, 13]. Although milling is a common intermediate machining process, Moehring et al. [14] showed that machining of additively manufactured geometries poses high demands on machine tools. A pentapod is well suited for this task due to its high rigidity. In this publication, a METROM PM700 is used.

Current manufacturing strategies follow a fixed sequence. In preliminary experiments, the process parameters of the additive process are determined and a prediction is made about the maximum number of layers $N_{max}$ that can be applied one after the other and about the reliably achievable layer thickness. [15] According to the preliminary experiments, at first $N_{max}$ layers are applied and then the uppermost layer is completely milled. After that, the next $N_{max}$ layers are applied, before the machining process is repeated. [7, 12, 13, 15] This sequence continues until the part is fully manufactured. Notwithstanding the process progress, a milling step is applied, in which the entire surface is machined. This approach has several disadvantages. For example, full-surface milling is not always necessary since deviations from the desired geometry usually only occur at certain points [16]. Furthermore, the milling process can be executed too late to correct build-up failures that have already occurred at previous layers. On the other hand, the execution of the milling process can be carried out too often and unnecessarily, since the estimation of the maximum number of layers $N_{max}$ is conservative for safety reasons. The negative effects can be reduced by using the milling process only when needed. Therefore, the height deviation between the desired and actual geometry can serve as a criterion for the use and the area of application of the milling process [17]. There are research studies that identify potential defect locations a priori from the model or the path planning using process simulations. During the manufacturing process these

locations are checked for height deviations at defined points, and if a height deviation is detected, it is reworked with a defined machining regime [16]. However, there is a risk of missing not process-related defects. Hence, Chen et al. [18, 19], Xu et al. [5], and Tang et al. [20] investigated methods for detecting geometric deviations from laser scans of the part surface.

In hybrid manufacturing systems currently available on the market, the manufacturing process is not monitored by the system [16, 21, 22]. It is not checked by the manufacturing system whether the conditions from the preliminary experiments, in which the process parameters were identified, are permanently adhered to during the manufacturing process. In the absence of automatic monitoring, the process sequence is not adjusted. This lack of robustness requires extensive preliminary experiments to keep the failure rate low. All the problems mentioned above lead to the conclusion in current research that monitoring the manufacturing process and a process control based on it is necessary and useful. This is done in order to increase the robustness of the manufacturing process. [4, 21–29]

To monitor the manufacturing process, it is necessary to measure the actual part geometry. Laser scanners are a suitable measuring device for these requirements and are industrially established. These sensors use the triangulation principle to measure distance. A static laser beam is widened into a line by a special optic and projected onto the part surface. With the help of a receiving optic, the diffusely reflected light is projected onto a sensor matrix. The distance to the surface and the position along the laser line can be calculated from the projection of the laser line on the sensor matrix [30]. In this way, a height profile along the laser line is determined. Laser scanners are used in the field of arc welding to determine the weld bead geometry [8, 31–33]. In addition, there are studies that use laser scanners to determine the surface quality of flat structures [20, 32, 34, 35]. In both cases, the laser scanner is moved in a linear motion over the object to be measured and the surface relief is then generated from the individual measurements.

## 2. METHODS AND SET-UP

### 2.1. PENTAPOD STRUCTURE AND RESULTING CONSTRAINTS

A pentapod, like the *METROM PM700* shown in Fig. 1a is a five-axis kinematic system. In this kinematic system, five threaded rods carry a freely movable tool spindle. Each threaded rod is connected at one end to the tool spindle and has a drive motor attached to the icosahedral enclosure by means of a cardanic mounting [36]. The drive is used to manipulate the distance between the tool spindle and the mounting, while the cardanic mounting of the motor allows the respective threaded rod to assume any orientation. Fig. 1b shows the design of the tool spindle. The tool spindle consists of a drive for the milling tool and one retaining ring and four swivel rings. A threaded rod is attached to each ring via a hinge joint. The milling tool drive is rigidly connected to the retaining ring, thus the angle of rotation $\varphi_{sp}$ of the spindle drive is related to the retaining ring. The four swivel rings are located at a fixed, defined distance from the retaining ring, but can rotate relative to each other and to the retaining ring as the tool spindle moves. Fig. 2a shows a top view of the drive arrangement.

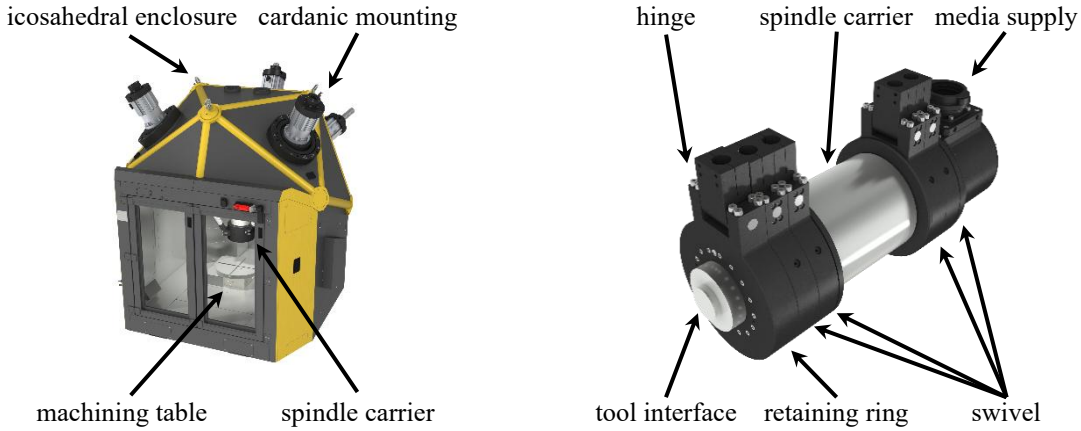


(a) Overview (b) Structure of tool spindle

Fig. 1. METROM PM700 mechanical structure

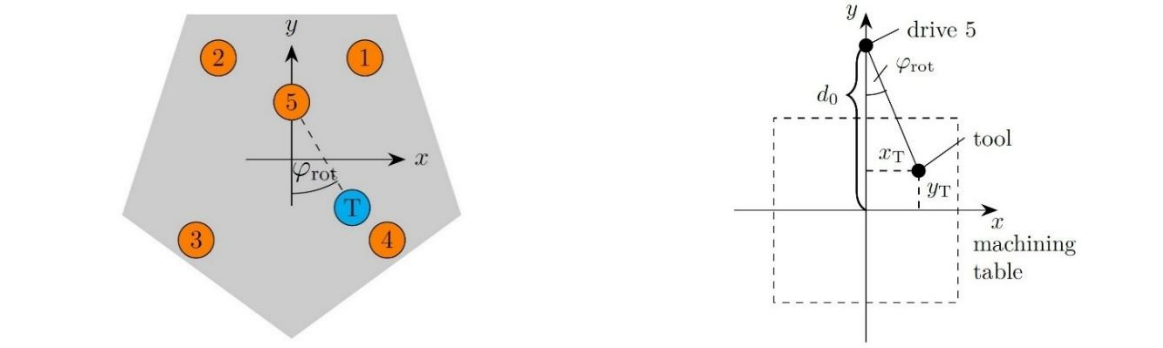


(a) METROM PM700 axis drives (1-5), tool (T) and machine frame definition (topview).

(b) Computation of forced rotation angle $\varphi_{rot}$; the machine frame is located in the center of the (square) machining table

Fig. 2. Definition and explanation of $\varphi_{rot}$

The retaining ring is linked to drive five, which is mounted in the *yz*-plane of the machine frame. The projection of the direction vector of the threaded rod of drive five into the *xy*-plane yields the orientation vector of the retaining ring (dashed line). The angle between the orientation vector and the *y*-axis corresponds to the forced rotation $\varphi_{rot}$ of the retaining ring. If the rotation axis of the tool spindle drive coincides with the *z*-axis of the machine frame, the tool spindle is in a vertical position above the frame origin and the orientation vector of the retaining ring points along the *y*-axis ($\varphi_{rot} = 0$). Fig. 2 shows that the orientation of the retaining ring $\varphi_{rot}$ depends on the position of the tool spindle in the workspace. This means that a movement which is not towards the radial direction of axis five implies a rotation of the retaining ring in the workspace due to the rigid coupling of the retaining ring and the drive through the threaded rod, and thus a change in its orientation. For milling purposes, this implicit rotation can be neglected. However, for proper laser scanner measurements, it is crucial to consider this position-dependent implicit rotation.

Assuming that the machine coordinate system is located at the center of the machining table and that $d_0$ is the distance between the center of the table and the drive five projected into the *xy*-plane, the rotation angle $\varphi_{rot}$ and thus the rotation angle $\varphi_{rot}$ and thus the rotation of

the tool can be calculated by $\varphi_{\text{rot}} = \arctan\left(\frac{x_\text{T}}{d_0 - y_\text{T}}\right)$ (see Fig. 2b). By normalizing the coordinates to the distance $d_0$ and limiting the interval $\frac{y_\text{T}}{d_0} \in [-1,1)$ based on geometric constraints, the following applies to the rotation angle

$$\varphi_{\text{rot}} = \arctan\left(\frac{\frac{x_\text{T}}{d_0}}{1 - \frac{y_\text{T}}{d_0}}\right) \text{ with } \frac{y_\text{T}}{d_0} \in [-1,1) \quad . \tag{1}$$

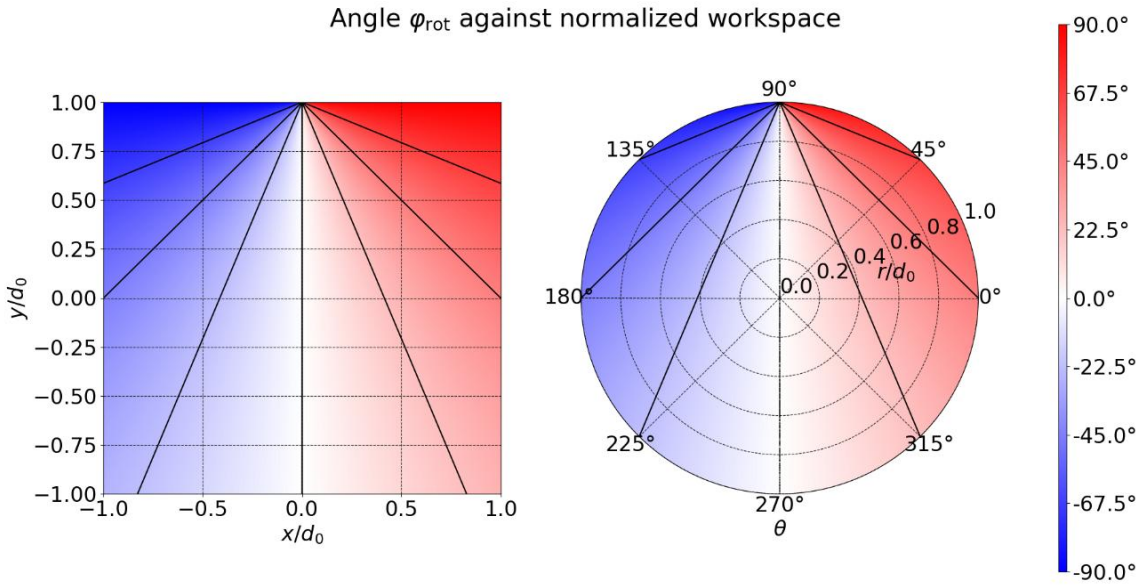


Fig. 3. Forced rotation angle $\varphi_{\text{rot}}$ in the normalized workspace. For a square machining table (left) it's a cartesian plot with $x$ and $y$ normalized by $d_0$ while for a round machining table (right) a polar plot with angle $\theta \in [-\pi,\pi)$ and normalized radius $r/d_0 \in [0,1]$ is used. The color indicates the rotation of the tool if it is located at the corresponding position. Positions with equivalent torsion are colored similarly. The black lines correspond to the color bar values.

For the intervals $\frac{y_\text{T}}{d_0} \in [-1,1)$ and $\frac{x_\text{T}}{d_0} \in [-1,1]$ the torsion is shown in Fig. 3. When utilizing a square machining table, the normalized workspace of the PM700 is approximately $\left|\frac{x_\text{T}}{d_0}\right| = \left|\frac{y_\text{T}}{d_0}\right| = 0.75$ resulting in a maximum rotation angle of $|\varphi_{\text{PM700}}| \approx 0.4\pi \approx 72°$ in the upper left and right corners.

## 2.2. FRAME DEFINITIONS AND HOMOGENEOUS COORDINATES

The following coordinate systems are requisite for the point cloud's stepwise calculation of the part measured by the laser scanner. These are always right-handed.

Cartesian coordinate systems whose base vectors are orthogonal to each other. The calculations of transformations between these coordinate systems are carried out in homogeneous coordinates [37]. Where:

| | |
|---|---|
| ${}^{k}\mathbf{p}$ | position vector in frame *k* |
| ${}^{k}\mathbf{p}_{O,i}$ | position vector of the origin of frame *i* represented in frame *k* |
| ${}^{k}\tilde{\mathbf{p}}$ | vector ${}^{k}\mathbf{p}$ as homogeneous vector ${}^{k}\tilde{\mathbf{p}} = \left[ {}^{k}\mathbf{p} \quad 1 \right]^{T}$ |
| ${}^{k}_{i}\mathbf{R}$ | rotation matrix; rotation of frame *i* w.r.t. *k*; a possible index denotes rotation axis and angle |
| ${}^{k}_{i}\mathbf{T}$ | transformation matrix; rotation and displacement of frame *i* w.r.t. *k* |

*Machine frame W (World)*

The machine frame *W* is the basis. Its origin is located in the centre of the top side of the machining table. The *y*-axis points in the direction towards the cardanic mounting five, the *z*-axis points vertically upwards along the *z*-axis of the machining table and the *x*-axis results from the right-handed system (see Fig. 2a). The *METROM PM700* provides its position data based on this coordinate system.

*Tool frame T (Tool)*

The tool frame *T* has its origin in the tool centre point (TCP), and the *z*-axis points from the TCP along the rotation axis of the spindle drive towards the retaining ring. In basic position, i.e. no rotations with respect to the machine frame *W* all three basis vectors of the frames *T* and *W* point in the same direction. The displacement and rotation of frame *T* relative to *W* is specified by three translatory position values *x*, *y* and *z* and two consecutive rotation angles $\varphi_C$ and $\varphi_A$. The angle $\varphi_C$ describes a rotation around the *z*-axis and the angle $\varphi_A$ describes a rotation around the *x*-axis of the system resulting from the rotation around the *z*-axis (consecutive rotation).

*Rotated tool frame $T_{rot}$ (rotated Tool)*

The rotated tool frame $T_{rot}$ has the same origin as the tool frame *T*, also the *z*-axes of the systems are identical. However, $T_{rot}$ is rotated with respect to *T* due to the constrained rotation by the angle $\varphi_{rot}$ (see Section 2.1). In addition, a further rotation can be forced by rotating the spindle axis by $\varphi_{sp}$.

*Ideal and real laser scanner frame $S_0$ and S (Sensor)*

The measurement of the sensor is oriented towards the *z*-axis of the tool coordinate system $T_{rot}$. For the used *MicroEpsilon scanControl LLT 3010-50/BL* laser scanner, the nominal measuring distance between the laser scanner and the measuring object is 125mm. This means that the TCP of the measuring tool, for which the path planning is done and whose position is provided by the machine, does not coincide with the reference point of the laser scanner measurements. The distance and the opposing orientation result in the necessity of introducing the ideal laser scanner frame $S_0$ in order to take this constraint into account. The origin of the sensor frame $S_0$ is therefore shifted by the nominal measurement distance with respect to the origin of the tool frame $T_{rot}$ (TCP) along the ${}^{T_{rot}}z$ -axis $\left({}^{T_{rot}}\mathbf{p}_{O,S_0} = [0 \quad 0 \quad 125\text{mm}]^{T}\right)$. Furthermore, it is defined that the *x*-axis of $S_0$ points towards the *y*-axis of $T_{rot}$, and the *y*-axis of $S_0$ results from the right-hand rule. The ideal laser scanner frame $S_0$ thus describes the orientation of the laser scanner based on a correctly manufactured mounting and considers geometric constraints resulting from the mounting position as well as sensor-specific constraints (see Fig. 4).

Figure 5 shows two design screenshots and an image of the laser scanner mount. For mounting the laser scanner, the HSK adapter and the two metal plates, dowel holes and dowel

pins are provided. However, manufacturing- and assembly-related deviations cannot be excluded.

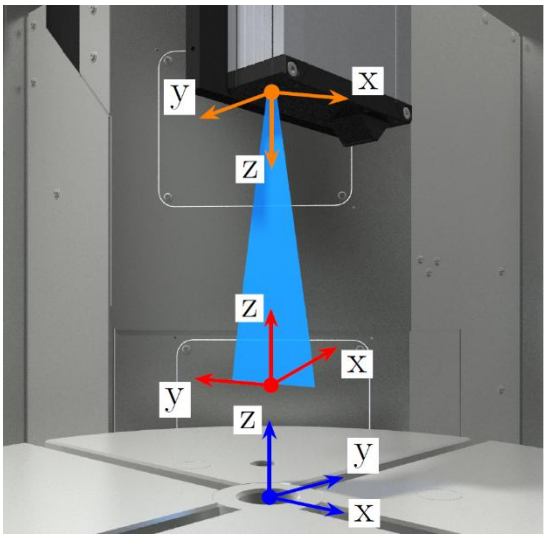


Fig. 4. Illustration of world frame $W$ (blue), rotated tool frame $T_{rot}$ (red), laserscanner frame $S_0$ (orange), their origins and their orientations. The rotation and displacement between $W$ and $T_{rot}$ is caused by the movement of the tool. The relationship between $T_{rot}$ and $S_0$ is fixed and results from the geometric boundary conditions.

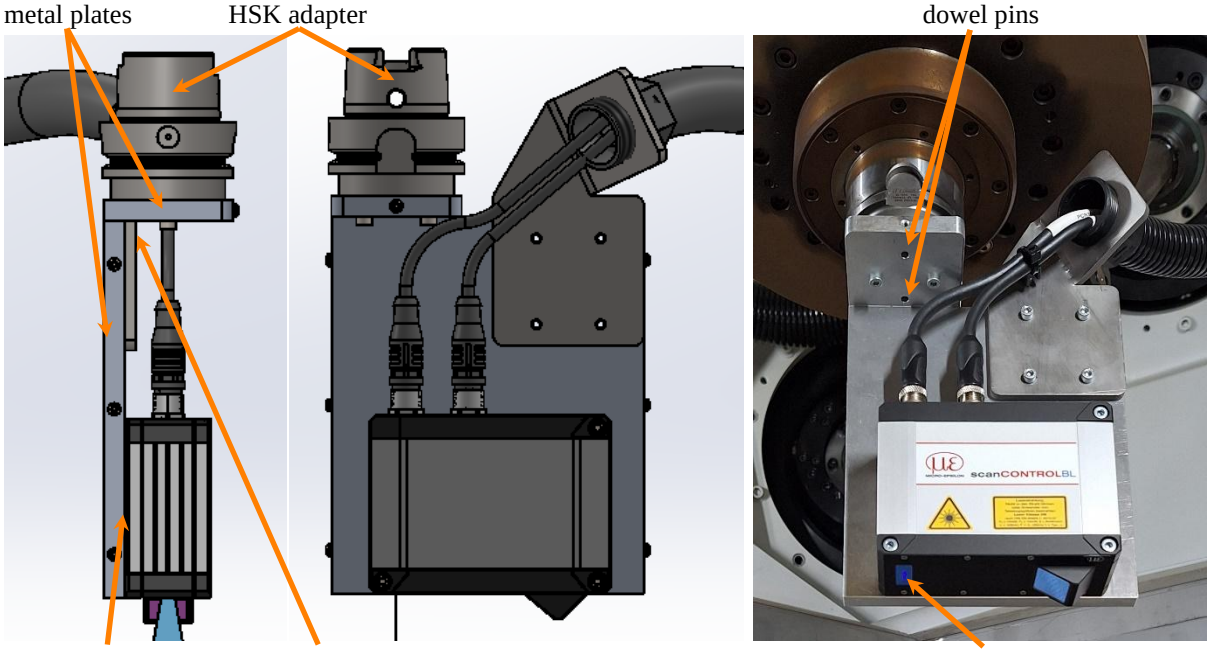


(a) left view (b) front view (c) picture of manufactured mounting

Fig. 5. Two screenshots of the CAD model and an image of the laser scanner mounting illustrate possible manufacturing and assembly tolerances, which may lead to a slight offset between the two laser scanner frames $S_0$ and $S$

Manufacturing-related deviations may include:

- component tolerances (e.g. the length of the HSK adapter),

- accuracy of the alignment holes, which may cause the HSK adapter to be misaligned,
- the 90° angle between the two metal plates.

In addition to manufacturing-related deviations, the following assembly-related deviations may occur:

- the tolerance of the laser scanner's mounting surface is not specified,
- the tolerance of the laser light's exit position relative to the mounting screws is not specified.

Due to the prior listed manufacturing and assembly tolerances of the laser scanner mounting, it must be assumed that the real laser scanner frame *S* of the laser scanner tool is slightly shifted and rotated with respect to the ideal laser scanner frame $S_0$, even if the offset is minimal and theoretical. Thus, the deviation between the two systems is not based on geometric constraints and is considered by transformation ${}^{S_0}_{S}\mathbf{T}$. This transformation has to be determined by calibration after the tool is mounted.

*Workpiece frame P (Piece)*

The workpiece frame *P* is the reference point for the workpiece itself. The workpiece is defined in this frame. Depending on the positioning on the machining table, there is an offset between *W* and *P*.

Figure 6 shows the frames and their relationship to each other.

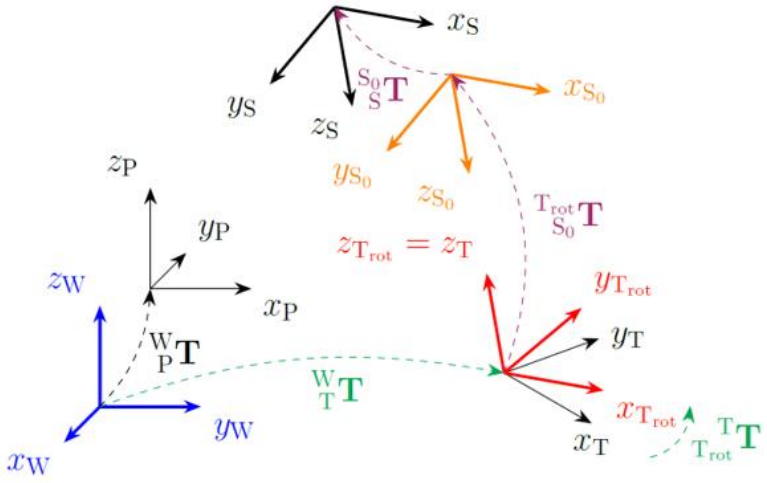


Fig. 6. Relationship between the frames and their corresponding transformations. The rotated tool frame (red) results from the world frame (blue) by applying the transformations ${}^{W}_{T}\mathbf{T}$ and ${}^{T}_{T_{rot}}\mathbf{T}$ (green) representing the movement and the forced tool rotation, whereas the laser scanner frames $S_0$ (orange) and S result from transformations ${}^{T_{rot}}_{S_0}\mathbf{T}$ and ${}^{S_0}_{S}\mathbf{T}$, respectively (violet)

## 2.3. DETERMINATION OF THE TRANSFORMATION MATRICES

### 2.3.1. BASIC POSITION

The position information provided by the machine refers to the basic position. This position is defined by the following constraints:

- the tool center point (TCP) is located in the origin of the machine frame $\left({}^{\mathrm{W}}x_{\mathrm{TCP}} = {}^{\mathrm{W}}y_{\mathrm{TCP}} = {}^{\mathrm{W}}z_{\mathrm{TCP}} = 0\right)$
  → the retaining ring is not twisted ($\varphi_{\mathrm{rot}} = 0$)
- the laser scanner is not tilted ($\varphi_{\mathrm{C}} = \varphi_{\mathrm{A}} = 0$)
- the *xz*-measurement plane of the laser scanner is congruent with the *yz*-plane of the machine frame *W*, the base vectors ${}^{\mathrm{S_0}}\mathbf{e}_{\mathrm{x}}$ and ${}^{\mathrm{T_{rot}}}\mathbf{e}_{\mathrm{y}}$ are antiparallel
  → this leads to the spindle angle $\varphi_{\mathrm{sp,0}}$ at which the frames $T_{\mathrm{rot}}$ and *T* are congruent
- the position and orientation of the workpiece in the workspace and thus ${}^{\mathrm{W}}_{\mathrm{P}}\mathbf{T}$ are known

Under the above conditions, the frames *W*, *T*, and $T_{\mathrm{rot}}$ coincide. Starting from this pose, a movement along the ${}^{\mathrm{W}}x$-axis would produce a 3D surface profile, since the direction of movement is perpendicular to the measurement plane of the laser scanner.

### 2.3.2. TRANSFORMATION SEQUENCE

The sequence of the applied transformation steps and the resulting transformation matrices are listed in Table 1.

Table 1. Transformation sequence and corresponding transformation matrix T.

| step | applied transformation | T |
|---|---|---|
| 1 | Rotation around *z*-axis ($\varphi_{\mathrm{C}}$) | |
| 2 | Rotation around *x*-axis ($\varphi_{\mathrm{A}}$) | ${}^{\mathrm{W}}_{\mathrm{T}}\mathbf{T}$ |
| 3 | Displacement (${}^{\mathrm{W}}\mathbf{p}_{\mathrm{O,T}}$) | |
| 4 | Forced Rotation around *z*-axis ($\varphi_{\mathrm{rot}}$) | ${}^{\mathrm{T}}_{\mathrm{T_{rot}}}\mathbf{T}$ |
| 5 | Rotation around spindle axis ($\varphi_{\mathrm{sp}}$) | |
| 6 | Displacement along *z*-axis (measuring distance of laser scanner) | |
| 7 | Rotation around *z*-axis ($-90^{\circ}$) | ${}^{\mathrm{T_{rot}}}_{\mathrm{S_0}}\mathbf{T}$ |
| 8 | Rotation around *x*-axis ($180^{\circ}$, Mirroring *z*-axis) | |
| 9 | Calibration | ${}^{\mathrm{S_0}}_{\mathrm{S}}\mathbf{T}$ |

The machine provides the rotation angles $\varphi_{\mathrm{C}}$, $\varphi_{\mathrm{A}}$ and the position vector ${}^{\mathrm{W}}\mathbf{p}_{\mathrm{O,T}} = \left[{}^{\mathrm{W}}x_{\mathrm{TCP}} \quad {}^{\mathrm{W}}y_{\mathrm{TCP}} \quad {}^{\mathrm{W}}z_{\mathrm{TCP}}\right]^{\mathrm{T}}$ to compute ${}^{\mathrm{W}}_{\mathrm{T}}\mathbf{T}$

$$ {}^{\mathrm{W}}_{\mathrm{T}}\mathbf{T} = \begin{bmatrix} \mathbf{R}_{\mathrm{x},\varphi_{\mathrm{A}}}\mathbf{R}_{\mathrm{x},\varphi_{\mathrm{C}}} & \mathbf{0} \\ \mathbf{0} & 1 \end{bmatrix}. \tag{2} $$

The rotation of the laser scanner caused by the forced rotation of the retaining ring $\varphi_{\mathrm{rot}}$ and by the spindle angle $\varphi_{\mathrm{sp}}$ together with $\Delta\varphi_{\mathrm{sp}} = \varphi_{\mathrm{sp}} - \varphi_{\mathrm{sp,0}}$ leads to the transformation matrix ${}^{\mathrm{T}}_{\mathrm{T_{rot}}}\mathbf{T}$

$$ {}^{\mathrm{T}}_{\mathrm{T_{rot}}}\mathbf{T} = \begin{bmatrix} \mathbf{R}_{\mathrm{z},\Delta\varphi_{\mathrm{sp}}}\mathbf{R}_{\mathrm{z},\varphi_{\mathrm{rot}}} & \mathbf{0} \\ \mathbf{0} & 1 \end{bmatrix}. \tag{3} $$

Transformation ${}^{\mathrm{T_{rot}}}_{\mathrm{S_0}}\mathbf{T}$ represents the constraints of the sensor itself. According to the transformation steps six to eight in Table 1 and a nominal measurement distance of 125 mm, ${}^{\mathrm{T_{rot}}}_{\mathrm{S_0}}\mathbf{T}$ can be denoted as:

$$ {}^{\mathrm{T_{rot}}}_{\mathrm{S_0}}\mathbf{T} = \begin{bmatrix} 0 & -1 & 0 & 0 \\ -1 & 0 & 0 & 0 \\ 0 & 0 & -1 & 125 \\ 0 & 0 & 0 & 1 \end{bmatrix}. \tag{4} $$

Equations (2) and (3) reveal that the two transformation matrices, ${}^{\mathrm{W}}_{\mathrm{T}}\mathbf{T}$ and ${}_{\mathrm{T_{rot}}}{}^{\mathrm{T}}\mathbf{T}$ are position-dependent. Therefore, these transformation matrices must be calculated from the position data for each measurement made, whereas ${}^{\mathrm{T_{rot}}}_{\mathrm{S_0}}\mathbf{T}$ and ${}^{\mathrm{S_0}}_{\mathrm{S}}\mathbf{T}$ are constant.

### 2.4. COMPUTATION OF THE POINT CLOUD

To compute the point cloud, each single laser scanner measurement has to be correlated with the position at which it was taken. Each single profile *k* consists of a defined number of measuring points and each measuring point *i* is represented by its (homogeneous) position vector in the laser scanner frame S

$$ {}^{\mathrm{S}}\mathbf{p}_{k,i} = \begin{bmatrix} {}^{\mathrm{S}}\mathrm{x}_{k,i} \\ 0 \\ {}^{\mathrm{S}}\mathrm{z}_{k,i} \end{bmatrix} \text{ resp. } {}^{\mathrm{S}}\tilde{\mathbf{p}}_{k,i} = \begin{bmatrix} {}^{\mathrm{S}}x_{k,i} \\ 0 \\ {}^{\mathrm{S}}z_{k,i} \\ 1 \end{bmatrix} \text{ with } k, i \in \mathbb{N}\,. \tag{5} $$

As the measurement is carried out in the *xz*-plane of the laser scanner, the *y*-component of the position vector is always zero. Therefore, ${}^{\mathrm{S}}\mathbf{p}_{k,i}$ is the position vector of the *i*th measuring point of the *k*th profile. By applying the constant transformation matrices ${}^{\mathrm{T_{rot}}}_{\mathrm{S_0}}\mathbf{T}$ and ${}^{\mathrm{S_0}}_{\mathrm{S}}\mathbf{T}$ the measuring point ${}^{\mathrm{S}}\tilde{\mathbf{p}}_{k,i}$ can be transformed from the laser scanner frame into the rotated tool frame. With the machine's position information, the position-dependent transformation matrices ${}^{\mathrm{W}}_{\mathrm{T}}\mathbf{T}_k$ and ${}_{\mathrm{T_{rot}}}{}^{\mathrm{T}}\mathbf{T}_k$ can be determined for each profile *k*. The transformation of each measuring point ${}^{\mathrm{S}}\tilde{\mathbf{p}}_{k,i}$ taken in the laser scanner frame *S* into the machine frame *W* can be expressed in concise form as a combination of all transformation matrices

$$ {}^{\mathrm{W}}\tilde{\mathbf{p}}_{k,i} = {}^{\mathrm{W}}_{\mathrm{T}}\mathbf{T}_k \; {}_{\mathrm{T_{rot}}}{}^{\mathrm{T}}\mathbf{T}_k \; {}^{\mathrm{T_{rot}}}_{\mathrm{S_0}}\mathbf{T} \; {}^{\mathrm{S_0}}_{\mathrm{S}}\mathbf{T} \; {}^{\mathrm{S}}\tilde{\mathbf{p}}_{k,i} = {}^{\mathrm{W}}_{\mathrm{S}}\mathbf{T}_k \; {}^{\mathrm{S}}\tilde{\mathbf{p}}_{k,i} \;. \tag{6} $$

In order to facilitate a comparison between the desired and the actual part geometry, the point cloud can be transferred into the workpiece frame *P* by applying the transformation ${}^{\mathrm{P}}_{\mathrm{W}}\mathbf{T}$ to ${}^{\mathrm{W}}\tilde{\mathbf{p}}_{k,i}$

## 3. RESULTS

The ensuing preliminary remarks are intended to facilitate the interpretation of the results. Table 2 provides a comprehensive list of the characteristic values for the respective components.

Individual profiles are captured during movement. This means that the laser scanner does not remain in one position during capture; instead, the measurements are triggered while moving. $v_m$ is the measurement tool velocity and $d_m$ describes the distance between two consecutive trigger pulses. The pulse frequency $f$ is technically limited to $f_{max} = 100Hz$ and the measurement tool velocity $v_m$ is limited by $v_{TCP,max}$ but for the intended use in additive manufacturing, a maximum measurement tool velocity of $v_{m,max} = 50mm/s = 3000mm/min$ is sufficient. The consecutive trigger distance $d_m$ depends on the desired point cloud resolution. The weld beads produced during arc welding are typically on the order of millimeters, and the geometries created with them are in the centimeter range or larger. Therefore, the range from 0.1mm to 1mm is suitable for $d_m$. Both parameters $v_m$ and $d_m$ can be chosen arbitrarily within their ranges as long as they do not exceed $f_{max}$

$$\frac{v_m}{d_m} \leq f_{max} \tag{7}$$

Small values of $v_m$ and $d_m$ lead to a high resolution but a long acquisition time, while high values result in a faster acquisition but a weaker resolution.

Table 2. Component characteristics

| Parameter | Symbol | Value |
|---|---|---|
| **METROM PM700** | | |
| Position accuracy | | ±10 µm |
| Repeatability | | 3 µm |
| Maximum TCP velocity (limited by control) | $v_{TCP,max}$ | 5000 mm/min |
| Maximum TCP acceleration (limited by control) | $a_{TCP,max}$ | 10 m/s² |
| Trigger pulses for laser scanner measurement (maximum) | $f_{max}$ | 100/s |
| **MicroEpsilon scanCONTROL LLT 3010-50/BL** | | |
| nominal measurement distance | $d_z$ | 125 mm |
| measurement range (relative to the nominal distance) | $\Delta d_z$ | ±20 mm |
| nominal measurement width (at nominal measurement distance) | $d_x$ | 50 mm |
| minimum measurement width (at minimum measurement distance) | $d_{x,min}$ | 43.3 mm |
| maximum measurement width (at maximum measurement distance) | $d_{x,max}$ | 56.5 mm |
| Line linearity (distance) | | 3 µm |
| Resolution | | up to 2048 |
| Wavelength | | 405 nm |
| **BLUM TC60** | | |
| Maximum probing speed | | 3000 mm/min |
| Repeatability ($2\sigma$) | | 0.3 µm |

For a qualitative evaluation of the height measurement, different gauge blocks (10 mm, 20 mm, 50 mm and 100 mm) were placed at five different positions on the square machining table, probed with a *BLUM TC60* touch probe, then recorded with the laser scanner ($v_m = 5\ \mathrm{mm\ s^{-1}}$, $d_m = 0.1\ \mathrm{mm}$), and the difference between the two measurements was determined. Fig. 7 shows a sketch of the setup. Table 3 summarizes the positions where the probe touched the gauge blocks and where the high information of the laser scan was evaluated. As depicted in Fig. 8, the comparison between probe measurement and laser scan shows deviations of up to 0.12 mm. To evaluate the accuracy in all three spatial directions, a rotationally symmetrical cone was positioned at the same five positions. This cone was also

measured with the touch probe and then recorded with the laser scanner ($v_m = 5$ mm s$^{-1}$, $d_m = 0.1$ mm). The open source application CloudCompare was used to determine the offset between the point cloud from the laser scanner measurement and the cone's CAD model, which is positioned based on the touch probe measurement. The results are shown in Table 4. Here, too, the deviation is within a maximum range of 0.12 mm. The measuring system can therefore be considered sufficiently accurate for the intended application in additive manufacturing.

Table 3. Test position coordinates and the start and end of the position-related scan path

| Position | Coordinates | | Scan path | |
|---|---|---|---|---|
| | x/[mm] | y/[mm] | Start | End |
| 1 | -25 | 15 | (-75/15) | (5/15) |
| 2 | -225 | 235 | (-275/235) | (-195/235) |
| 3 | 225 | 235 | (195/235) | (275/235) |
| 4 | 225 | -235 | (195/-235) | (275/-235) |
| 5 | -225 | -235 | (-275/-235) | (-195/-235) |

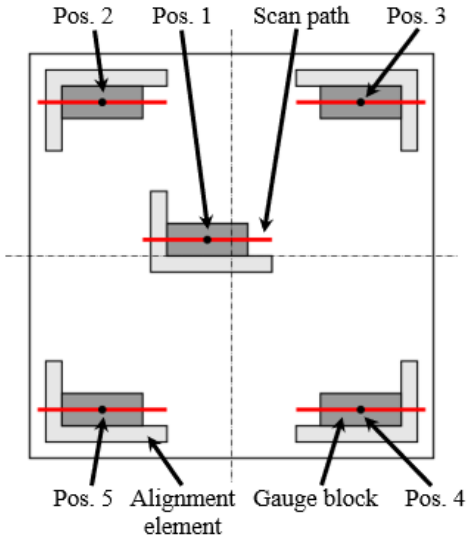


Fig. 7. A sketch of the test setup showing the five dedicated test positions, where the gauge blocks and the cone were placed

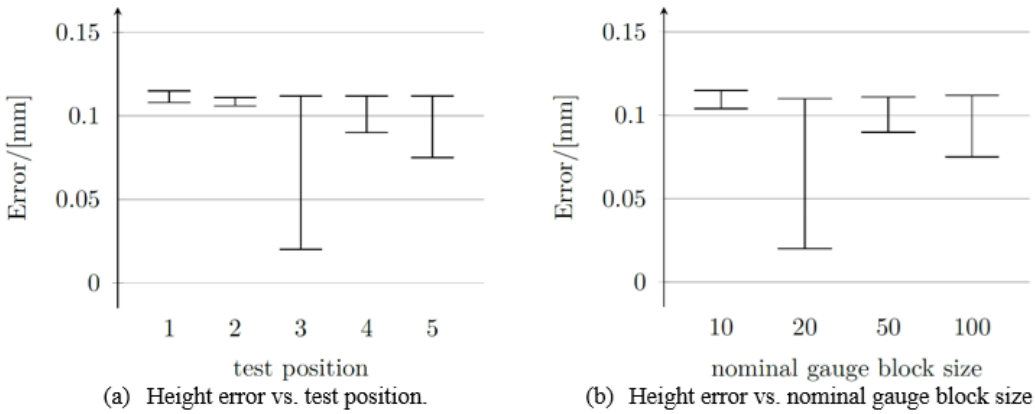


(a) Height error vs. test position. (b) Height error vs. nominal gauge block size

Fig. 8. Evaluation of gauge block height measurement

Table 4. Cone position measurement results.

| Error in | Error in [mm] at test position | | | | |
|---|---|---|---|---|---|
| | 1 | 2 | 3 | 4 | 5 |
| x | 0.122 | 0.123 | 0.080 | -0.010 | 0.120 |
| y | 0.107 | 0.017 | 0.070 | 0.049 | 0.041 |
| z | -0.014 | 0.130 | 0.073 | 0.000 | 0.073 |

The effect of the two parameters, measurement speed $v_m$ and distance between two consecutive trigger pulses $d_m$, on the quality of the measurement is shown in Fig. 9 and 10. For this purpose, the rotationally symmetrical cone was measured at different speeds $v_m$ and different pulse distances $d_m$, and the deviation from the position recorded with a touch probe was plotted. While the pulse distance $d_m$ has no negative influence on accuracy, the deviation increases with increasing measuring speed $v_m$. The measurement was carried out at different velocities along the x-axis, which is why the deviation in the x-direction varies, while the deviation in the other two axes remains constant. This is due to the uncertainty of the position determination at the time a measurement is triggered. The causes for this are controller-related and cannot be remedied by the application or minimized arbitrarily.

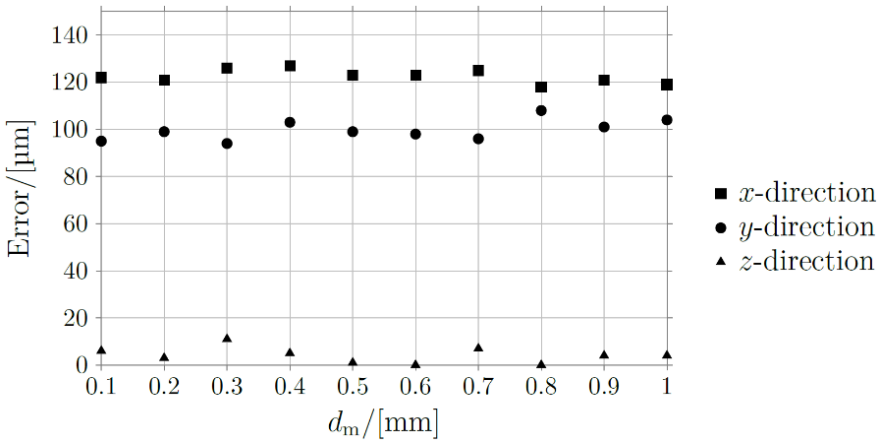


Fig. 9. Correlation between measurement error and pulse distance $d_m$ ($v_m$ = 5 mm s$^{-1}$)

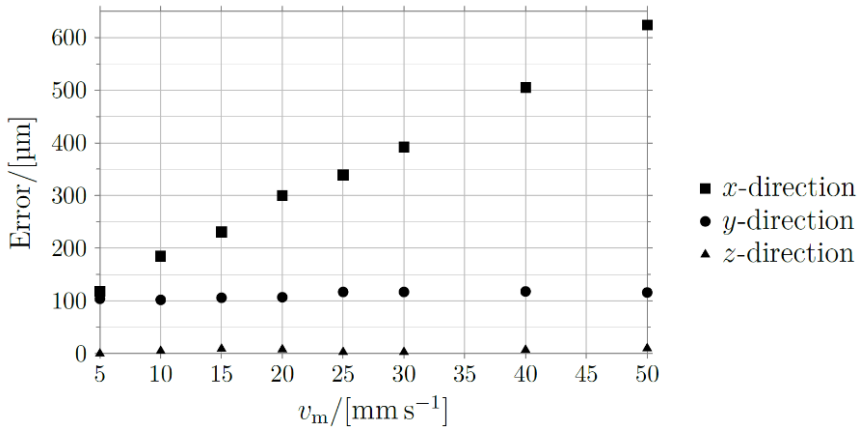


Fig. 10. Correlation between measurement error and measurement velocity $v_m$ (measurement along x-axis, $d_m$ = 0.5 mm)

## 4. SUMMARY

This publication presents a concept for the integration of a laser scanner into an additive manufacturing system based on a multi-axis kinematic in the form of a pentapod. The kinematic features of the drive concept and the resulting consequences for the point cloud generation are explained. The application of the homogeneous coordinate transformation to generate a point cloud from the raw data was shown, along with the step-by-step procedure for calculating the transformations from the machine data and the geometric constraints. Finally, the accuracy achieved by the laser scanner measurements was discussed. By considering the mechanical constraints, the pentapod was successfully expanded to include a laser scanner. This will facilitate a more responsive approach to the additive manufacturing process in the future.

ACKNOWLEDGEMENTS

Supported by:


on the basis of a decision
by the German Bundestag

The research project "Derivation of quality criteria for adaptive process control in arc-based hybrid manufacturing (AdaptWAAM)" is funded by the Federal Ministry of Economic Affairs and Energy as part of the "Industrial Collective Research" program on the basis of a resolution of the German Bundestag. This project 01IF22758N from the "Forschungsvereinigung Schweißen und verwandte Verfahren e.V. des DVS", Dusseldorf, is carried out at the "Chair of Joining Technology and Assembly" at the Dresden University of Technology.

REFERENCES

[1] ISO/ASTM 52900:2021, *Additive Manufacturing – General Principles – Fundamentals and Vocabulary*, International Organization for Standardization, Geneva, CH.
[2] ID H., 2017, *Development and Implementation of Metals Additive Manufacturing*, Badiru AB, Valencia VV, Liu D, (Eds.), Additive Manufacturing Handbook, CRC Press, 215–224.
[3] BALIDAS A., KERBRAT O., HASCOET J-Y., 2024, *The Potential of Additive Manufacturing of Metal Components to Reduce Environmental Impacts*, Journal of Machine Engineering 24/2, 94–104.
[4] WILLIAMS S.W, MARTINA F., ADDISON AC., DING J., PARDAL G., COLEGROVE P., 2016, *Wire + Arc Additive Manufacturing*, Materials Science and Technology 32/7, 641–7.
[5] XU P., YAO X., CHEN L., ZHAO C., LIU K., MOON S.K., BI G., 2022, *In-Process Adaptive Dimension Correction Strategy for Laser Aided Additive Manufacturing Using Laser Line Scanning*, Journal of Materials Processing Technology, 303, 117544.
[6] ANDRADE DG, ZHU C., BAMBY HE., MONTEIRO K., SABARI S., BABU R., DA SIMÕES SILVA L., TANKOVA T., 2026, *Characterisation of Infill Strategies in WAAM for Solid Components Fabricated with ER100S-G Wire*, Int. J. Adv. Manuf. Technol., 143/5-6, 3239–59.
[7] SURYAKUMAR S., KARUNAKARAN KP., BERNARD A., CHANDRASEKHAR U., RAGHAVENDER N., SHARMA D., 2011, *Weld Bead Modeling and Process Optimization in Hybrid Layered Manufacturing*, Computer-Aided Design 43/4, 331–44.
[8] HU Z., QIN X., LI Y., YUAN J., WU Q., 2020, *Multi-Bead Overlapping Model with Varying Cross-Section Profile for Robotic GMAW-Based Additive Manufacturing*, Journal of Intelligent Manufacturing 31/5, 1133–47.
[9] RAFFAELI R., LETTORI J., PELLICCIARI M., 2025, *Geometric Modeling of Overlapped WAAM Beads by Hermite Curves*, Rapid Prototyping Journal, 31/11, 364–85.
[10] FOORGINEJAD A., ZAREI M., EMAM SM., HOSSEINI BAGHDADABADI SMJ., 2026, *A Novel Multi-Bead Overlapping Model for Wire Arc Additive Manufacturing (WAAM) Processes with Dissimilar Beads Area Strategy*, Int. J. Adv. Manuf. Technol., 142/1-2, 309–28.

[11] RAUCH M., PIEDRA DORADO J., HASCOET J-Y., RUCKERT G., 2021, *A Novel Method for Additive Manufacturing of Complex Shape Curved Parts by Using Variable Height Layers*, Journal of Machine Engineering, 21/3, 80-91, https://doi.org/10.36897/jme/138820.
[12] AKULA S., KARUNAKARAN KP., 2006, *Hybrid Adaptive Layer Manufacturing: an Intelligent Art of Direct Metal Rapid Tooling Process*, Robotics and Computer-Integrated Manufacturing 22/2, 113–23.
[13] LI F., CHEN S., SHI J., TIAN H., ZHAO Y., 2017, *Evaluation and Optimization of a Hybrid Manufacturing Process Combining Wire Arc Additive Manufacturing with Milling for the Fabrication of Stiffened Panels*, Applied Sciences 7/12, 1233.
[14] MOEHRING H-C., MAUCHER C., BECKER D., STEHLE T., EISSELER R., 2023, *The Additive-Subtractive Process Chain - a Review*, Journal of Machine Engineering, 23/1, 5–35, https://doi.org/10.36897/jme/162041.
[15] JAFARI D., VANEKER T.H.J., GIBSON I., 2021, *Wire and Arc Additive Manufacturing: Opportunities and Challenges to Control the Quality and Accuracy of Manufactured Parts*, Materials & Design, 202, 109471.
[16] MA G., ZHAO G., LI Z., YANG M., XIAO W., 2019, *Optimization Strategies for Robotic Additive and Subtractive Manufacturing of Large and High Thin-Walled Aluminum Structures*, The International Journal of Advanced Manufacturing Technology 101/5, 1275–92.
[17] DING D., PAN Z., CUIURI D., LI H., 2015, *Wire-Feed Additive Manufacturing of Metal Components: Technologies, Developments and Future Interests*, The International Journal of Advanced Manufacturing Technology 81/1, 465–81.
[18] CHEN L., YAO X., XU P., MOON S.K., BI G., 2021, *Rapid Surface Defect Identification for Additive Manufacturing with In-Situ Point Cloud Processing and Machine Learning*, Virtual and Physical Prototyping 16/1, 50–67.
[19] CHEN L., YAO X., XU P., MOON S.K., ZHOU W., BI G., 2023, *In-Process Sensing, Monitoring and Adaptive Control for Intelligent Laser-Aided Additive Manufacturing*, Chen S, Zhang Y, Feng Z, (Eds.). Transactions on Intelligent Welding Manufacturing, Volume IV No. 2 2020, 1st ed. Springer Nature Singapore, Imprint Springer. Singapore, 3–30.
[20] TANG S., WANG G., ZHANG H., 2019, *In Situ 3D Monitoring and Control of Geometric Signatures in Wire and Arc Additive Manufacturing*, Surface Topography: Metrology and Properties 7/2, 25013.
[21] WU B., PAN Z., DING D., CUIURI D., LI H., XU J., NORRISH J., 2018, *A Review of the Wire Arc Additive Manufacturing of Metals: Properties, Defects and Quality Improvement*, Journal of Manufacturing Processes, 35, 127–39.
[22] XIA C., PAN Z., POLDEN J., LI H., XU Y., CHEN S., ZHANG Y., 2020, *A Review on Wire Arc Additive Manufacturing: Monitoring, Control and a Framework of Automated System*, Journal of Manufacturing Systems 57, 31–45.
[23] BEAMAN J.J., ATWOOD C., BERGMAN T.L., BOURELL D., HOLLISTER S., ROSEN D., 2004, *Additive/Subtractive Manufacturing Research and Development in Europe*. https://apps.dtic.mil/sti/citations/ADA466756 (accessed on 04.11.2021).
[24] CHABOT A., RAUCH M., HASCOËT J-Y., 2019, *Towards a Multi-Sensor Monitoring Methodology for AM Metallic Processes*, Welding in the World, 63/3, 759–69.
[25] DAS B., SAHOO N., PATEL P., GHOSH A., KHAN M.A., BHUSHAN B., MADAN R., SHRIVASTAVA P., MSOMI V., 2026, *Wire Arc Additive Manufacturing (WAAM): a Comprehensive Review of Process, Materials, Modelling, Artificial Intelligence, and Industrial Applications*, Journal of Alloys and Compounds 1058, 186347.
[26] EVERTON S.K., HIRSCH M., STRAVROULAKIS P., LEACH R.K., CLARE A.T., 2016, *Review of In-Situ Process Monitoring and In-Situ Metrology for Metal Additive Manufacturing*, Materials & Design 95, 431–45.
[27] LIU J., XU Y., GE Y., HOU Z., CHEN S., 2020, *Wire and Arc Additive Manufacturing of Metal Components: a Review of Recent Research Developments*, The International Journal of Advanced Manufacturing Technology 111/1, 149–98.
[28] XU F., DHOKIA V., COLEGROVE P., MCANDREW A., WILLIAMS S., HENSTRIDGE A., NEWMAN S.T., 2018, *Realisation of a Multi-Sensor Framework for Process Monitoring of the Wire Arc Additive Manufacturing in Producing Ti-6Al-4V Parts*, International Journal of Computer Integrated Manufacturing, 31/8, 785–98.
[29] ZHANG Y., CHEN Y., LI P., MALE A.T., 2003, *Weld Deposition-Based Rapid Prototyping: A Preliminary Study*, Journal of Materials Processing Technology, 135/2, 347–57.
[30] DING Y., ZHANG X., KOVACEVIC R., 2016, *A Laser-Based Machine Vision Measurement System for Laser Forming*, Measurement, 82, 345–54.
[31] ARTAZA T., ALBERDI A., MURUA M., GORROTXATEGI J., FRIAS J., PUERTAS G., MELCHOR M.A., MUGICA D., SUAREZ A., 2017, *Design and Integration of WAAM Technology and in Situ Monitoring System in a Gantry Machine*, Procedia Manufacturing, 13, 778–85.

[32] CUI J., YUAN L., COMMINS P., HE F., WANG J., PAN Z., 2021, *WAAM Process for Metal Block Structure Parts Based on Mixed Heat Input*, The International Journal of Advanced Manufacturing Technology, 113/1, 503–21.
[33] LI Y., SUN Y., HAN Q., ZHANG G., HORVATH I., 2018, *Enhanced Beads Overlapping Model for Wire and Arc Additive Manufacturing of Multi-Layer Multi-Bead Metallic Parts*, Journal of Materials Processing Technology, 252, 838–48.
[34] HERALIC A., 2012, *Monitoring and Control of Robotized Laser Metal-Wire Deposition*, Chalmers Univ. of Technology, Göteborg.
[35] XIONG J., LI Y-J., YIN Z-Q., CHEN H., 2018, *Determination of Surface Roughness in Wire and Arc Additive Manufacturing Based on Laser Vision Sensing*, Chinese Journal of Mechanical Engineering, 31/1, 74.
[36] NEUGEBAUER R., SCHWAAR M., IHLENFELDT ST., PRITSCHOW G., EPPLER C., GARBER T., 2002, *New Approaches to Machine Structures to Overcome the Limits of Classical Parallel Structures*, CIRP Annals, 51/1, 293–6.
[37] CRAIG J.J., 2005, *Introduction to Robotics: Mechanics and Control*, 3rd ed. Pearson Prentice Hall, Upper Saddle River, NJ.